

Coherent Visible-Light-Generation Enhancement in Silicon-Based Nanoplasmonic Waveguides via Third-Harmonic Conversion

S. Sederberg* and A. Y. Elezzabi

Ultrafast Optics and Nanophotonics Research Laboratory, University of Alberta, Edmonton, Alberta T6G 2V4, Canada
(Received 12 November 2014; published 4 June 2015)

We report visible third-harmonic conversion at $\lambda = 517$ nm in subwavelength silicon-based nanoplasmonic waveguides at an unprecedented conversion efficiency of 2.3×10^{-5} . This marks both the highest third-harmonic conversion efficiency in a silicon-based or nanoplasmonic structure and the smallest silicon waveguide structure demonstrated to date. The high conversion efficiency is attributed to tight electric field confinement and strong light-matter coupling arising from surface plasmon modes in the nanoplasmonic waveguide, enabling efficient nonlinear optical mixing over micrometer length scales. The nonresonant geometry of the waveguide enables the entire $\lambda = 1550$ nm femtosecond pulse spectrum to be converted to its third harmonic, which may be easily extended to the entire visible spectrum. We envisage that third-harmonic generation in silicon-based nanoplasmonic waveguides could provide a platform for integrated, broadband visible light sources and entangled triplet photons on future hybrid electronic-silicon photonic chips.

DOI: [10.1103/PhysRevLett.114.227401](https://doi.org/10.1103/PhysRevLett.114.227401)

PACS numbers: 78.67.-n, 42.65.Ky, 42.65.Wi, 73.20.Mf

Understanding the potential for efficient frequency conversion in nano-optical circuits is of key importance for future chip-scale information processing. Optical harmonic generation marked the beginning of nonlinear optics and it remains a powerful process for converting coherent optical radiation to higher frequencies [1]. In the particle interpretation of light, harmonic generation is understood as the union of N low-energy photons into a single photon with $N \times$ the energy. For example, third-harmonic generation (THG) occurs when three photons of the fundamental frequency ω interact in a nonlinear medium to generate one photon at the 3ω frequency. In the wave description of THG, a driving electric field E_ω induces a third-order electric polarization in a medium that acts as a 3ω radiation source as follows [2]:

$$P^{(3)}(3\omega) = \frac{\epsilon_0}{4} \chi^{(3)}(-3\omega; \omega, \omega, \omega) E_\omega^3, \quad (1)$$

where $\chi^{(3)}(-3\omega; \omega, \omega, \omega)$ is the third-order electric susceptibility and ϵ_0 is the permittivity of free space. Although second-harmonic generation (SHG) is only possible in materials without inversion symmetry, THG occurs in any nonlinear medium for sufficient electric field strength.

Typically, high-efficiency harmonic generation is achieved in exotic crystals that are incompatible with modern semiconductor processing, making implementation in planar photonic circuitry a challenge. As a critical material for electronics, Si has also become the foundation for integrated optical systems, and it merges electronics, photonics, and nanoplasmonics on a single platform. The potential of Si as a functional nonlinear optical material has incited many nonlinear frequency conversion studies,

including stimulated Raman scattering, self- and cross-phase modulation, and four-wave mixing [3]. Although a variety of optical functionalities have been demonstrated in Si, efficient light generation remains challenging due to its indirect band gap. Rather than endeavor light emission through phonon-assisted transitions from the valence band to the conduction band, it is more feasible to generate coherent light through nonlinear optical interactions such as THG [2]. Temporal pulse compression in dispersion engineered Si photonic waveguides offers a potential means to improve the THG conversion efficiency to $\sim 10^{-7}$ [4]. However, photonic waveguides are bulky compared to modern electronic circuitry and it is desirable to reduce them to the nanoscale, permitting unidimensional interfacing to electronic circuits.

Despite decades of development, efficient SHG and THG in nanoscale structures remains a formidable challenge. Nanoplasmonic structures incorporate metallic features, allowing propagating optical signals to couple strongly to the conduction electrons of the metal, enabling subwavelength optical confinement [5]. Confinement of input radiation to a nanoscale volume not only facilitates compact frequency conversion structures suitable for planar optical circuitry, but also enhances the optical intensity, increasing nonlinear frequency conversion efficiencies. Although “plasmonic” metals are characterized by large $\chi^{(3)}$ coefficients (e.g., $\chi^{(3)} \sim 0.2 \text{ nm}^2 \text{ V}^{-2}$ for gold [6]), high losses restrict nonlinear interactions to the metallic surfaces where few nonlinear dipoles contribute to the 3ω signal, resulting in low conversion efficiencies. Furthermore, previous investigations of THG in plasmonic structures, such as aperture arrays and gratings, have not been conducive to integration in planar photonic circuits [7–14]. For example, rough silver films on a Si substrate have been shown to enhance

THG conversion efficiencies compared to a thick silver film [7]. However, such films are not nanoscale devices and no absolute measurement of the THG conversion efficiency was reported. Nanoplasmonic waveguides can be easily loaded with a high-nonlinearity material, enabling plasmonically enhanced nonlinear interactions in the volume (rather than the surface) of a nonlinear subwavelength structure. Specifically, a Si-loaded nanoplasmonic waveguide ($\chi^{(3)} = 0.19 \text{ nm}^2 \text{ V}^{-2}$ for Si [15]) would enable high-efficiency THG in waveguides with sub-100-nm dimensions, delivering a compact visible light source for all-optical signal processing and quantum information encoding [16–18].

In this Letter, we present the first demonstration of THG in a nanoplasmonic waveguide. Broadband THG in the green spectral region is generated in a Si-based nanoplasmonic waveguide that is simple to fabricate, compatible with modern electronics and photonics technologies, and occupies an ultracompact footprint of $0.40 \mu\text{m}^2$. Femtosecond laser pulses at $\lambda = 1550 \text{ nm}$ with input powers in the range of $85 \mu\text{W}$ – 1.52 mW are used to generate strong THG with conversion efficiencies up to 2.3×10^{-5} , the highest reported to date in any Si-based device or nanoplasmonic structure. The nonresonant waveguide enables 3ω up-conversion of the entire pulse spectrum, which can be extended to a much wider spectral range [19]. These results demonstrate a unique, enabling platform for integrated frequency conversion sources spanning visible to near-IR wavelengths.

We investigate a nanoplasmonic waveguide that consists of a Si core with width $w = 95 \text{ nm}$, height $h = 340 \text{ nm}$, length $L = 5 \mu\text{m}$, and a $t = 60 \text{ nm}$ thick gold cap, as shown in Fig. 1(a). Because of the subdiffraction dimensions of the nanoplasmonic waveguide, only a single quasi-TM waveguide mode at $\lambda = 1550 \text{ nm}$ exists. The effective refractive index n_{eff} of the waveguide mode is plotted versus wavelength between 1500 and 1600 nm in Fig. 1(b) and decreases from 2.71 to 2.63 over this range. The third harmonic of $\lambda = 1550 \text{ nm}$ lies in the green region of the visible spectrum where the photon energy, $E_{3\omega} = 2.40 \text{ eV}$, exceeds the indirect band gap energy of Si, $E_g = 1.1 \text{ eV}$.

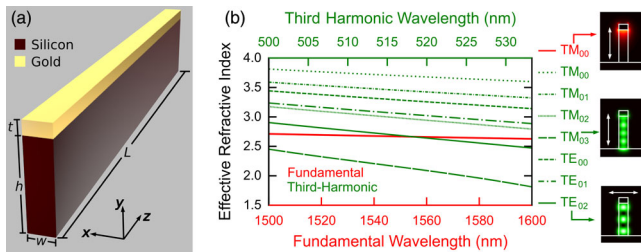


FIG. 1 (color online). (a) Schematic depiction of the silicon-based nanoplasmonic waveguide. (b) Mode dispersion curves for the fundamental and 3ω wavelengths. Time-averaged intensity distributions ($|I|$) for three waveguide modes are shown on the right-hand side.

This observation comes with two important consequences: the 3ω signal will be absorbed strongly and high dispersion in Si will hinder phase matching. Four quasi-TM and three quasi-TE modes exist for the 3ω signal, and n_{eff} for each of these modes is also plotted in Fig. 1(b). Strong dispersion of the Si core produces a higher n_{eff} for the low-order 3ω modes than the fundamental mode. For higher-order 3ω modes, more energy propagates outside of the high-index Si core, resulting in a lower n_{eff} . Although the dispersion relations of the $\text{TE}_{02}^{3\omega}$ and TM_{00}^{ω} modes intersect at $\lambda = 1552 \text{ nm}$, we will demonstrate through simulations that phase matching between these two modes is not possible because the TM_{00}^{ω} cannot excite the $\text{TE}_{02}^{3\omega}$ mode.

It is also important to consider the relevant length scales of each waveguide mode. At $\lambda = 1550 \text{ nm}$, the TM_{00}^{ω} mode has an effective wavelength, $\lambda_{\text{eff}}^{\omega} = 581 \text{ nm}$, and decays by a factor of e^{-1} as it propagates, $L_{\text{prop}}^{\omega} = 3.1 \mu\text{m}$ (loss = $1.4 \text{ dB}/\mu\text{m}$). The tight mode confinement and short propagation length signify strong light-matter coupling and are ideal for efficient nonlinear interactions in an ultracompact structure. Similarly, the $\text{TM}_{00}^{3\omega}$ mode has $\lambda_{\text{eff}}^{3\omega, \text{TM}_{00}} = 140 \text{ nm}$ and propagates a characteristic length, $L_{\text{prop}}^{3\omega, \text{TM}_{00}} = 634 \text{ nm}$ ($1.1\lambda_{\text{eff}}^{\omega}$), demonstrating that phase matching over multiple wavelength scales is not feasible. For comparison, the $\text{TM}_{03}^{3\omega}$ mode has $\lambda_{\text{eff}}^{3\omega, \text{TM}_{03}} = 235 \text{ nm}$ and propagates a characteristic length $L_{\text{prop}}^{3\omega, \text{TM}_{03}} = 260 \text{ nm}$ ($0.45\lambda_{\text{eff}}^{\omega}$). For similar reasons, previous observation of THG in bulk Si has been measured from surface reflection, where the 3ω signal is generated within the absorption depth of both ω and 3ω [20–26]. Although this nanoplasmonic structure does not provide the benefits of phase matching, it enables 3ω up-conversion of broadband femtosecond pulses with minimal spectral amplitude modulation.

To gain fundamental insight into the generation and propagation dynamics of the 3ω radiation, we incorporate a third-order polarization into finite-difference time-domain simulations, via Eq. (1). Linear losses and $\chi^{(3)}$ values for Si, Au, and SiO_2 are taken from prior experimental measurements [6,15,27–29]. We propagate pulses of $\tau_p = 84 \text{ fs}$ duration centered at $\lambda = 1550 \text{ nm}$ through the Si-based nanoplasmonic waveguide depicted in Fig. 1(a) and characterize the resulting THG signal. A snapshot of the E_y electric field of the 3ω signal taken at the arrival time of the pulse peak is shown in Fig. 2(a). As expected, the most efficient THG occurs where the fundamental radiation is the most intense, near the Si-Au interface and close to the waveguide input facet ($z = 0.31 \mu\text{m}$) [30]. Based on the intrinsic dielectric losses at 3ω , the skin depth of Si is $\delta_{\text{Si}} = 723 \text{ nm}$, whereas the skin depth of Au is $\delta_{\text{Au}} = 18.9 \text{ nm}$. Therefore, any 3ω that is radiated in the direction of the Au film ($t = 60 \text{ nm}$) will either be reflected into the Si or absorbed in the Au. Any 3ω that is radiated into the Si core will contribute to the propagating 3ω

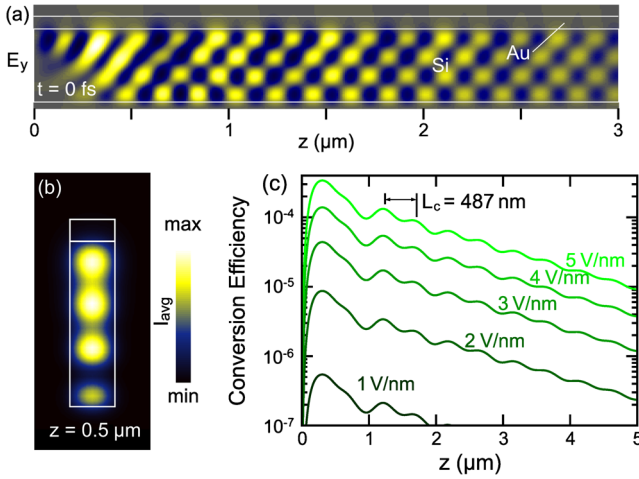


FIG. 2 (color online). (a) Time snapshot of the $3\omega E_y$ electric field at the fundamental pulse peak arrival. (b) Time-averaged intensity distribution of the 3ω radiation at $z = 0.5 \mu\text{m}$. (c) Third-harmonic conversion efficiency along the waveguide z axis for peak electric fields of $E_{\text{peak}}^\omega = 1, 2, 3, 4,$ and 5 V/nm .

waveguide mode. A time-averaged intensity distribution in the $z = 0.5 \mu\text{m}$ plane is shown in Fig. 2(b), depicting the mode transformation from a field localized to the Au-Si interface into a distribution that resembles the $\text{TM}_{03}^{3\omega}$ mode. By recording the fundamental and 3ω power transmission through each plane of the waveguide, the THG conversion efficiency η^{THG} is calculated for several peak electric fields, as shown in Fig. 2(c). The maximum η^{THG} is observed at $z = 310 \text{ nm}$ from the input facet and decreases along the z axis of the waveguide. For $E_{\text{peak}}^\omega = 5 \text{ V/nm}$, conversion efficiencies up to $\eta = 1.40 \times 10^{-4}$ are calculated. Oscillations in η^{THG} with a period of $L_c = 487 \text{ nm}$ occur along the length of the waveguide, which closely matches the coherence length $L_c = 2\pi/\Delta k = 505 \text{ nm}$ predicted from the n_{eff} data in Fig. 1(b) for a pure $\text{TM}_{03}^{3\omega}$ mode. Evidently, phase matching is not sufficient to compensate for the high 3ω losses. Setting $\chi^{(3)} = 0$ for Au and SiO_2 reveals that 98.9% of the THG occurs in the Si, demonstrating that loading nanoplasmonic waveguides with a highly nonlinear medium drastically increases η^{THG} over a bare nanoplasmonic structure.

To accurately measure THG in a Si-based nanoplasmonic waveguide, it is crucial to directly excite nonlinearities in the waveguide so that the measurements are not intertwined with nonlinear excitations in an on-chip coupling scheme. By direct collinear coupling of free-space $\lambda = 1550 \text{ nm}$ radiation into the nanoplasmonic waveguides using a microscope objective and outcoupling the generated visible emission with a lensed single-mode optical fiber (SMF), detailed spectral analysis and direct extraction of the THG conversion efficiency become possible. When considering a very short nanoplasmonic waveguide, the substrate must be reduced to $\leq 10 \mu\text{m}$ dimensions, which is

practically challenging and a special scheme must be realized. As such, the nanoplasmonic waveguides are fabricated on a narrow ridge that is etched to a depth $d_{\text{etch}} = 75 \mu\text{m}$, allowing for collinear access with standard microscope objectives and lensed SMFs [30]. An artistic rendering of the sample along with the excitation and detection scheme are shown in Fig. 3(a). Figure 3(b) presents a SEM of a single Si-based nanoplasmonic waveguide. A narrow ridge including several nanoplasmonic waveguides embedded in silica cladding is shown in Fig. 3(c), and the inset depicts a cross-sectional SEM of a nanoplasmonic waveguide end facet. Cross-sectional dimensions of the Si core are measured to be $w \times h = 95 \text{ nm} \times 340 \text{ nm}$ and the gold cap has a thickness of $t = 60 \text{ nm}$.

Free-space radiation from a laser emitting $\tau_p = 84 \text{ fs}$ pulses centered at $\lambda = 1550 \text{ nm}$ is collinearly coupled into the nanoplasmonic waveguides using a microscope objective (N.A. = 0.85). For peak input powers above $P_{\text{peak}}^\omega = 9.9 \text{ W}$, bright visible light emission is observed from the waveguides under normal room lighting. Visible emission collected from above the sample by a $20\times$ microscope objective and delivered to a charge-coupled device camera is shown in Fig. 3(d). Bright white light emission with a strong blue component is visible at the input facet of the nanoplasmonic waveguide and distinct THG (green light) is observed at the output facet. Depending on input excitation alignment and power, strong white light emission could be observed along the entire length of the waveguide. The white light emission arises

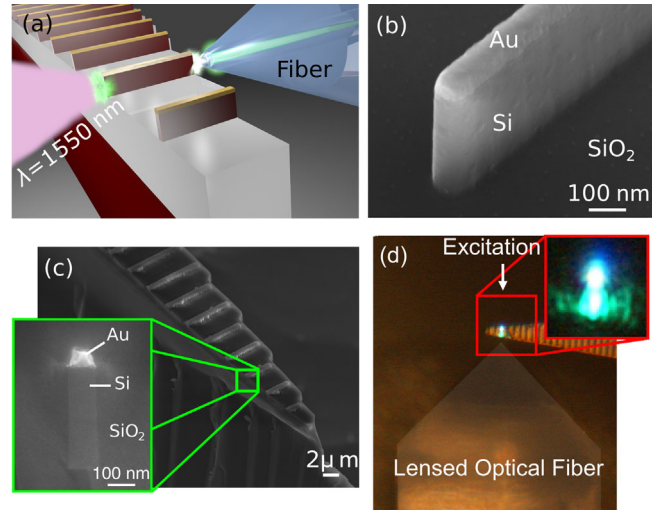


FIG. 3 (color online). (a) Schematic depiction of the conceived device, excitation scheme, and observed visible emission. (b) SEM of a single nanoplasmonic waveguide before deposition of a SiO_2 cladding. (c) SEM of several nanoplasmonic waveguides fabricated on a narrow beam. A close-up of the cross-sectional geometry of the waveguide end facet is shown in the inset. (d) Optical microscope image of visible light emission from the nanoplasmonic waveguides.

from collisions between hot electrons and valence electrons close to the input facet of the nanoplasmonic waveguide, where a two-photon absorption-generated free-carrier population interacts with the tightly confined nanoplasmonic mode. These free-carriers can be ponderomotively accelerated to energies exceeding the threshold for impact ionization in Si, leading to avalanche multiplication of the free-carrier population [31]. Although interesting, white light emission from hot electrons is not a coherent light source and is not investigated in these measurements. We optimize the input alignment conditions for the strongest THG signal, which reduces the white light emission considerably. Movie S1 in the Supplemental Material [30] presents THG from several individual nanoplasmonic waveguides as the beam is scanned across, demonstrating that emission was only observed from waveguides and not from other areas of the sample. The THG signal was present in every nanoplasmonic waveguide that was tested regardless of the waveguide length.

The coherent light emission spectrum is measured by coupling both the ω and 3ω light emitted from the output facet of the nanoplasmonic waveguide to a lensed SMF. Figure 4(a) depicts the outcoupled laser spectrum together with the 3ω spectrum, which spans a wavelength range of $500 \leq \lambda \leq 530$ nm. The broad 3ω spectrum and absence of sharp peaks confirm that phase matching does not play a role in the THG. The 3ω spectrum as calculated from the measured fundamental spectrum is also shown for

reference. The excellent agreement between the calculated and the measured 3ω spectra further confirms the absence of phase matching. Similar measurements on a bare Si photonic waveguide produce a similar THG signal strength, confirming that the dominant nonlinear response arises from the Si features. However, the THG signal from the Si-based nanoplasmonic waveguide is approximately 27% stronger in a footprint area that is reduced by over a factor of 3 [30].

A surface plot depicting the 3ω spectral power $P_{\text{out}}^{3\omega}$ as a function of the average input laser power P_{in}^{ω} is shown in Fig. 4(b). Regardless of P_{in}^{ω} , the 3ω spectrum spans $500 \leq \lambda \leq 530$ nm, and the peak wavelength is at $\lambda = 517$ nm. The overlaid plot conveys a measured 3ω spectrum for $P_{\text{in}}^{\omega} = 1.36$ mW (dashed line in the figure). As shown in Fig. 4(c), a log-log plot of the P_{in}^{ω} versus the total 3ω power $P_{\text{out}}^{3\omega}$ (obtained by integrating the 3ω spectrum) scales with a slope of 2.99 ± 0.02 . Similarly, the slopes for specific wavelengths in the 3ω spectrum, $\lambda = (512, 517, 520)$ nm, are found to be $3.04 \pm 0.01, 2.93 \pm 0.01$, and 3.16 ± 0.04 , respectively. The $P_{\text{out}}^{3\omega} \propto (P_{\text{in}}^{\omega})^3$ dependence confirms that the green light originates from the third-order $\chi^{(3)}(-3\omega; \omega, \omega, \omega)$ nonlinear optical interaction [2] and demonstrates that the entire 3ω spectrum grows uniformly with increasing input power.

Using a calibrated spectrometer detector, an absolute measure of the 3ω power and conversion efficiency is obtained. The THG conversion efficiency from the nanoplasmonic structure is plotted as a function of the input power on a log-log scale in Fig. 4(d). A linear fit to this data produces a line with a slope of 3.84, which is very close to the expected value of 4. This quartic power scaling arises from the expected 3ω conversion efficiency dependence, i.e., $P_{\text{out}}^{3\omega}/P_{\text{in}}^{\omega} \propto (E_{\text{in}}^{\omega})^4$. For a peak electric field of $E_{\text{peak}}^{\omega} = 4.8$ V/nm, the conversion efficiency is measured to be $\eta^{\text{THG}} = 2.3 \times 10^{-5}$ and green light powers up to $P_{\text{out}}^{3\omega} = 35$ nW are generated. For reference, the calculated η^{THG} is plotted on the same graph, for two physical scenarios: perfectly smooth Au films and Au films with nanoscale roughness that would enhance the average electric fields by an additional factor of 1.09. The scaling trend for an electric field enhancement of 1.09 matches the experimental measurements very closely and, therefore, the roughness of the Au film cannot be neglected. Finally, we also plot an estimate of the maximum internal conversion efficiency in the nanoplasmonic waveguides. From this, we extract the maximum internal conversion efficiency in the experiments to be $\eta^{\text{THG}} = 4.71 \times 10^{-4}$.

The measured $\eta^{\text{THG}} = 2.3 \times 10^{-5}$ marks a 400 \times increase in η^{THG} over previous plasmonic arrays [10], a 230 \times increase in η^{THG} over bulky silicon photonic structures [4], and a $\sim 10^6 \times$ increase over SHG efficiencies in a single plasmonic structure [32]. Remarkably, this high η^{THG} is demonstrated in an ultracompact device footprint of

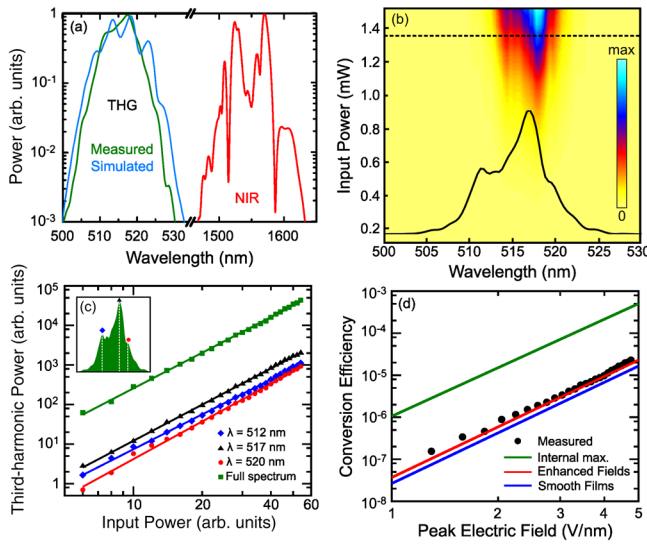


FIG. 4 (color online). (a) Spectra of the fundamental (red), the measured third harmonic (green), and the third harmonic calculated from the fundamental spectrum (blue). (b) Surface depicting third-harmonic power versus wavelength and input power. The black overlaid 3ω spectrum is measured for $P_{\text{in}}^{\omega} = 1.36$ mW. (c) Log-log plots of detected 3ω power versus input power for the entire spectrum (green) and individual wavelengths, $\lambda = (512, 517, 520)$ nm. (d) Third-harmonic conversion efficiency as a function of peak electric field.

0.40 μm^2 , with potential for further reduction. The absence of saturation in the $P_{\text{out}}^{3\omega} \propto (P_{\text{in}}^{\omega})^3$ trend or damage to the sample demonstrate that η^{THG} can be increased further simply by increasing the input power. We note that further increases in the input power will eventually lead to depletion of the fundamental pulses due to two-photon absorption. For example, the critical free-carrier density in Si of $n_c = 1.44 \times 10^{21} \text{ cm}^{-3}$ is reached for an electric field of $E = 2.2 \text{ V/nm}$. The fact that we do not yet observe saturation in η^{THG} is due to the short interaction length in the nanoplasmonic waveguide and the near-instantaneous nature of the THG process. Furthermore, the nonresonant characteristics of the Si-based nanoplasmonic waveguide enable the visible light color to be tuned by simply changing the excitation wavelength, where an excitation wavelength of $\lambda^{\omega} = 1200 \text{ nm}$ would generate violet light and $\lambda^{\omega} = 2100 \text{ nm}$ would generate red light. The compatibility of these structures with electronics and photonics processing techniques make them ideal for monolithic integration with existing technologies. We note that military specification electronic circuits use Au interconnects, and it is anticipated that integration of Au features into CMOS electronics would not affect electronic performance. Alternatively, CMOS-compatible plasmonic materials, such as Al or TiN, could replace the Au features.

In summary, we have demonstrated dramatic increases in the third-harmonic conversion efficiency in Si-based nanoplasmonic waveguides. Absorption of the third-harmonic signal in the Si waveguide core enables uniform conversion of broadband femtosecond pulses. These measurements are performed in a nanoscale, Si-based structure, making it attractive for use in Si photonic or electronic circuitry. The conceptual simplicity of this design leaves room for tailoring the waveguide geometry to further enhance the conversion efficiency, with the possibility of achieving integrated coherent visible light sources with microwatt powers. These results demonstrate the feasibility for conversion of near-IR radiation to visible radiation with technologically significant efficiencies, enabling nanoscale Si-based visible light sources on a chip.

This work was supported by the Natural Sciences and Engineering Research Council of Canada and Alberta Innovates.

*Present Address: Max-Planck-Institute of Quantum Optics, Hans-Kopfermann-Strasse 1, 85748 Garching, Germany

- [1] P. Franken, A. Hill, C. Peters, and G. Weinreich, Generation of Optical Harmonics, *Phys. Rev. Lett.* **7**, 118 (1961).
- [2] P.N. Butcher and D. Cotter, *The Elements of Nonlinear Optics* (Cambridge University Press, Cambridge, England, 1990).
- [3] R. Dekker, N. Usechak, M. Först, and A. Driessen, Ultrafast nonlinear all-optical processes in silicon-on-insulator waveguides, *J. Phys. D* **40**, R249 (2007).
- [4] B. Corcoran, C. Monat, C. Grillet, D.J. Moss, B.J. Eggleton, T.P. White, L. O'Faolain, and T.F. Krauss, Green light emission in silicon through slow-light enhanced third-harmonic generation in photonic-crystal waveguides, *Nat. Photonics* **3**, 206 (2009).
- [5] S.A. Maier, *Plasmonics: Fundamentals and Applications* (Springer, New York, 2007).
- [6] S. Palomba, H. Harutyunyan, J. Renger, R. Quidant, N.F. van Hulst, and L. Novotny, Nonlinear plasmonics at planar metal surfaces, *Phil. Trans. R. Soc. A* **369**, 3497 (2011).
- [7] E.M. Kim, S.S. Elovikov, T.V. Murzina, A.A. Nikulin, O.A. Aktsipetrov, M.A. Bader, and G. Marowsky, Surface-Enhanced Optical Third-Harmonic Generation in Ag Island Films, *Phys. Rev. Lett.* **95**, 227402 (2005).
- [8] M. Lippitz, M.A. van Dijk, and M. Orrit, Third-harmonic generation from single gold nanoparticles, *Nano Lett.* **5**, 799 (2005).
- [9] A.V. Andreev, A.A. Korneev, L.S. Mukina, M.M. Nazarov, I.R. Prudnikov, and A.P. Shkurinov, Simultaneous generation of second and third optical harmonics on a metal grating, *Phys. Rev. B* **74**, 235421 (2006).
- [10] T. Xu, X. Jiao, and S. Blair, Third-harmonic generation from arrays of sub-wavelength metal apertures, *Opt. Express* **17**, 23582 (2009).
- [11] G.X. Li, T. Li, H. Liu, S.M. Wang, S.N. Zhu, and K.W. Cheah, Spectral analysis of enhanced third harmonic generation from plasmonic excitations, *Appl. Phys. Lett.* **98**, 261909 (2011).
- [12] T.V. Murzina, I.A. Kolmychek, K. Wouters, T. Verbiest, and O.A. Aktsipetrov, Plasmon-assisted enhancement of third-order nonlinear optical effects in core (shell) nanoparticles, *J. Opt. Soc. Am. B* **29**, 138 (2012).
- [13] T. Hanke, J. Cesar, V. Knittel, A. Trügler, U. Hohenester, A. Leitenstorfer, and R. Bratschich, Tailoring spatiotemporal light confinement in single plasmonic nanoantennas, *Nano Lett.* **12**, 992 (2012).
- [14] B. Metzger, M. Hentschel, M. Lippitz, and H. Giessen, Third-harmonic spectroscopy and modeling of the nonlinear response of plasmonic nanoantennas, *Opt. Lett.* **37**, 4741 (2012).
- [15] M. Dinu, F. Quochi, and H. Garcia, Third-order nonlinearities in silicon at telecom wavelengths, *Appl. Phys. Lett.* **82**, 2954 (2003).
- [16] S. Sederberg, V. Van, and A.Y. Elezzabi, Monolithic integration of plasmonic waveguides into a complimentary metal-oxide-semiconductor- and photonic-compatible platform, *Appl. Phys. Lett.* **96**, 121101 (2010).
- [17] D.J. Dikken, M. Spasenovic, E. Verhagen, D. van Oosten, and L. Kuipers, Characterization of bending losses for curved plasmonic nanowire waveguides, *Opt. Express* **18**, 16112 (2010).
- [18] J.A. Dionne, L.A. Sweatlock, M.T. Sheldon, A.P. Alivisatos, and H.A. Atwater, Silicon-based plasmonic for on-chip photonics, *IEEE J. Sel. Top. Quantum Electron.* **16**, 295 (2010).
- [19] T. Carmon and K.J. Vahala, Visible continuous emission from a silica microphotonic device by third-harmonic generation, *Nat. Phys.* **3**, 430 (2007).

- [20] N. Bloembergen, W. K. Burns, and M. Matsuoka, Reflected third-harmonic generated by picosecond laser pulses, *Opt. Commun.* **1**, 195 (1969).
- [21] W. K. Burns and N. Bloembergen, Third-harmonic generation in absorbing media of cubic or anisotropic symmetry, *Phys. Rev. B* **4**, 3437 (1971).
- [22] C. C. Wang, J. Bomback, W. T. Donlon, C. R. Huo, and J. V. James, Optical Third-Harmonic Generation in Reflection from Crystalline and Amorphous Samples of Silicon,” *Phys. Rev. Lett.* **57**, 1647 (1986).
- [23] D. J. Moss, H. M. van Driel, and J. E. Sipe, Third-harmonic generation as a structural diagnosis of ion-implanted amorphous and crystalline silicon, *Appl. Phys. Lett.* **48**, 1150 (1986).
- [24] D. J. Moss, H. M. van Driel, and J. E. Sipe, Dispersion in the anisotropy of optical third-harmonic generation in silicon, *Opt. Lett.* **14**, 57 (1989).
- [25] E. C. Fox and H. M. van Driel, Third harmonic generation as a structural probe of ion-implanted silicon, *IEEE J. Quantum Electron.* **25**, 1104 (1989).
- [26] G. Lüpke, D. J. Bottomley, and H. M. van Driel, Second- and third-harmonic generation from cubic centrosymmetric crystals with vicinal faces: Phenomenological theory and experiment, *J. Opt. Soc. Am. B* **11**, 33 (1994).
- [27] P. B. Johnson and R. W. Christy, Optical constants of the noble metals, *Phys. Rev. B* **6**, 4370 (1972).
- [28] E. D. Palik, *Handbook of Optical Constants* (Academic Press, New York, 1985).
- [29] K. S. Kim, R. H. Stolen, W. A. Reed, and K. W. Quoi, Measurement of the nonlinear index of silica-core and dispersion-shifted fibers, *Opt. Lett.* **19**, 257 (1994).
- [30] See Supplemental Material at <http://link.aps.org/supplemental/10.1103/PhysRevLett.114.227401> for descriptions of the nanofabrication process, calculation of the theoretical third-harmonic spectrum, spectrometer calibration procedures, estimation of the fundamental electric field strength, further details of the full-wave simulations, and measurements from bare Si photonic waveguides.
- [31] S. Sederberg and A. Y. Elezzabi, Ponderomotive Electron Acceleration in a Silicon-Based Nanoplasmonic Waveguide, *Phys. Rev. Lett.* **113**, 167401 (2014).
- [32] W. Cai, A. P. Vasudev, and M. L. Brongersma, Electrically controlled nonlinear generation of light with plasmonics, *Science* **333**, 1720 (2011).